High-density and low-density gas diffusion layers for proton exchange membrane fuel cells: Comparison of mechanical and transport properties

Liusheng Xiao [a], *Miaoqi Bian* [a], *Lijun Zhu* [b], *Kangjun Duan* [b], *Wenliang Leng* [b], *Roswitha Zeis* [d,e], *Pang-Chieh Sui* [b,c,**], *Houcheng Zhang* [f,*]

[a] *Faculty of Maritime and Transportation, Ningbo University, Ningbo, 315211, China*
[b] *School of Automotive Engineering, Wuhan University of Technology, Wuhan, 430070, China*
[c] *Foshan Xianhu Laboratory of the Advanced Energy Science and Technology Guangdong Laboratory*
[d] *Helmholtz Institute Ulm, Karlsruhe Institute of Technology, Ulm, 89081, Germany*
[e] *Zentrum für Sonnenenergie-und Wasserstoff-Forschung, Ulm, 89071, Germany*
[f] *Department of Microelectronic Science and Engineering, Ningbo University, Ningbo, 315211, China*

HIGHLIGHTS

- XCT, LBM and PSM are combined to compute porosity, diffusivity and permeability.
- SEM and compression tests are applied to investigate the mechanical strength.
- Thermal conductivity and electrical resistivity under different compression ratios are measured.
- Mechanical and transport properties of two types of GDL are comprehensively compared.

GRAPHICAL ABSTRACT

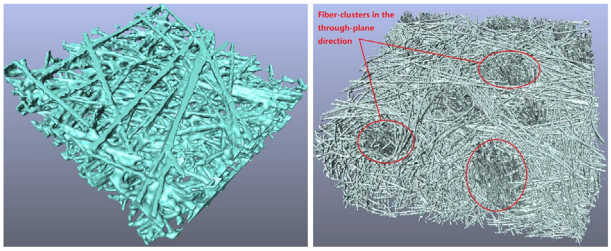

High Density (carbon paper) vs Low Density (carbon felt) GDLs

ABSTRACT

Gas diffusion layers (GDL) play multi-roles in proton exchange membrane fuel cells, including gas-water transport, thermal-electron conduction and mechanical support. Mechanical strength and transport properties are essential for GDLs. In this work, high-density (paper-type) and low density (felt-type) GDLs are scanned and reconstructed using X-ray computed tomography. Porosities under different compression ratios are compared and discussed. Effective diffusivity and liquid water permeability are calculated using pore-scale modeling and lattice Boltzmann method. Mechanical strength,

* *Corresponding author*.
** *Corresponding author*: School of Automotive Engineering, Wuhan University of Technology, Wuhan, 430070, China.
E-mail addresses: pcsui@whut.edu.cn (P.-C. Sui), zhanghoucheng@nbu.edu.cn (H. Zhang).

Keywords:
Paper-type GDL
Felt-type GDL
X-ray computed tomography
Conductivity measurement
Pore-scale modeling
Lattice Boltzmann method

anisotropic thermal-electrical resistivity for two types of GDLs are obtained using compression tests and thermal-electrical conductivity measurements. Results show that the porosity, diffusivity, permeability, and through-plane thermal-electrical conductivity of felt-type GDL are significantly higher than that of paper-type GDL owing to the higher porosity and fiber-clusters oriented along the through-plane direction. The in-plane electrical resistivity of paper-type GDL is lower than that of felt-type GDL. The mechanical strength of felt-type GDL is much lower, but the fibers of paper-type GDL are more easily to be broken because of its lower elasticity. The results obtained may guide microstructure optimization and performance improvement of GDLs.

Introduction

Proton exchange membrane fuel cell (PEMFC) is generally regarded as one of the most promising sustainable techniques owing to its high efficiency and zero emission. As one of the key porous components of PEMFC, a gas diffusion layer (GDL) located between the bipolar plate (BPP) and catalyst layer (CL) undertakes multiple roles, including gas-water transport, electron-thermal conduction, etc. In addition, GDLs also provide mechanical support for the membrane coated with CLs.

Felt-type and paper-type GDLs are the most widely used GDLs in PEMFCs. The main difference between them is the microstructural characteristics determined by different fabricating techniques. The fibers of the paper-type GDL are oriented along the in-plane (IP) direction layer by layer, and the fibers of the felt-type GDL are highly entangled and distributed in both the through-plane (TP) and IP directions [1,2]. The permeability of felt-type GDL is much higher [3], which results in a better performance for water transport. Fishman et al. [4] employed X-ray computed tomography (XCT) to compare the felt-type GDL and paper-type GDL. More homogenous porosity distribution was found in the felt-type GDL owing to the process of hydroentanglement, which was further supported by other authors [5,6]. Escribano et al. [7] found that the felt-type GDL showed higher elasticity during continuous compression cycles compared to the paper-type GDL. In addition, the felt-type GDL had more obvious isotropic microstructure in the IP and TP directions, which was supported and proved by scan electron microscope (SEM) [8]. Banerjee et al. [6] found that the local porosity distribution of felt-type GDL was more even, but the fibers were compressed to intrude the gas channel more easily. Recently, some studies investigated the mechanical properties of GDLs [9–11] and membranes [12–14]. These works mentioned above focused on the microstructural characterization and mechanical performance, while transport properties of the paper-type GDL and felt-type GDL have not been studied and compared yet, including the diffusivity, permeability, thermal conductivity and electrical resistivity in the TP and IP directions.

It is significant to comprehensively evaluate the overall performance of GDLs by comparing microstructural characteristics, transport properties and mechanical strength of the paper-type and felt-type GDLs. Some researchers applied experiments and simulation techniques to characterize and reconstruct the microstructure of GDLs by XCT [15–20], and then investigated the transport properties, such as the gas diffusivity [21–27], permeability [28–31], water flow [32–36], and thermal-electrical conductivity [37–46]. The liquid water transport was investigated [47–49] and enhanced through laser structured GDLs [50], perforated GDLs [51], micro elliptical groove GDLs [52], and coupling manipulation of pore structure and hydrophobicity [53]. The interplay between the water capillary transport and species diffusion was simulated [54], which showed the importance of an appropriate design for GDLs. Recently, some studies investigated the effects of compression on the mechanical integrity [55] and liquid water transport properties [56,57]. These research works only compared one or two of the transport properties for GDLs, which is not comprehensive enough to evaluate and design a new GDL with higher performance.

Based on both the experiment and simulation techniques, we propose an approach that combines SEM, XCT, compression tests, thermal conductivity measurements, electrical resistivity measurements, pore scale modeling (PSM) and lattice Boltzmann method (LBM) to characterize, scan and reconstruct three-dimensional (3D) GDL models. The stress-strain response, thermal conductivity, electrical resistivity, gas diffusivity and liquid water permeability between the paper-type and felt-type GDLs under different compression ratios (CRs) are compared. The compression ratio is defined as the ratio of compression distance with respect to the original GDL thickness.

The objective of this study is to conduct a comprehensive study for comparing the mechanical strength and transport properties between the high-density (paper-type) and low density (felt-type) GDLs under different CRs, which can guide microstructural optimization and performance improvement of GDLs. The specific objectives are given as follows:

(1) Combine XCT, LBM and PSM to compute the porosity, diffusivity and permeability of the felt-type and paper-type GDLs under different CRs.
(2) Apply SEM and compression tests to investigate the mechanical strength of the paper-type and felt-type GDLs.
(3) Conduct conductivity measurements to study the impacts of CRs on the thermal-electrical conductivities of the felt-type and paper-type GDLs.

(4) Compare the mechanical strength and transport properties between the felt-type and paper-type GDLs.

Experimental methods

In this section, experimental methods used for high-density (paper-type) and low density (felt-type) GDLs are introduced, including the sample preparation, XCT texts and thermal-electrical conductivity measurements. These experiments are completed in Zentrum für Sonnenenergie und Wasserstoff-Forschung (ZSW), Germany, and the repeating experiments are conducted to make these measurements more accurate. The samples are paper-type GDLs (SGL 39AA, SIGRACELL® company, Germany) and felt-type GDLs (SGL GFD 2.5, SIGRACELL® company, Germany). The diameter of the samples for XCT texts is 10 mm. The diameter of the samples for the compression tests is 30 mm. The diameter of the samples for the thermal conductivity measurements is 22 mm. The diameter of the samples for the electrical resistivity measurements in the TP direction is 26 mm. The size of the rectangular samples for the electrical resistivity measurements in the IP direction is 66 mm × 28 mm.

The diameters of the carbon fiber for the high-density (paper-type) and low-density (felt-type) GDLs are 8 and 11 μm, respectively. The porosities of the high-density and low-density GDLs are 0.78 and 0.95, respectively. The bulk densities of the high-density and low-density GDLs are 0.17 and 0.11 g/cm3, respectively. The mean pore diameters of the high-density and low-density GDLs are 43 and 65 μm, respectively. The thicknesses of the high-density and low-density GDLs are 300 and 2500 μm, respectively. The thickness of the felt-type GDL is not a commonly used value, but this type of GDLs with fiber-clusters in the through-plane direction can be fabricated with thinner thickness and higher bulk density. The comparison between two types of GDLs can guide better microstructural design by combing the advantages between them.

Fig. 1 (a) shows the XCT device combing with the compression setup, which are employed to compress, scan and reconstruct the microstructures of the paper-type and felt-type GDLs under different CRs. The GDL samples are scanned by the XCT device with the energy level of 36 kV, the source electric current of 222 μA, and the rotating steps of 0.2°. Thereafter, the two-dimensional (2D) greyscale images with a resolution of 2.99 μm are obtained. These images are further used for thresholding segmentation to distinguish fiber material and air phase. At last, 3D microstructures of the paper-type and felt-type GDL with CR = 0% are numerically reconstructed, as respectively shown in Fig. 1(b) and (c). The fibers are mainly oriented along the IP direction for the paper-type GDL, while some fiber-clusters are oriented along the TP direction for the felt-type GDL.

The conductivity experiments are performed to measure the thermal conductivity in the TP direction and the electrical resistivity in the TP and IP directions for the paper-type and felt-type GDL under different CRs. Fig. 2(a), (b) and (c) schematically show the principles of TP thermal conductivity, TP and IP electrical resistivity measurements, respectively.

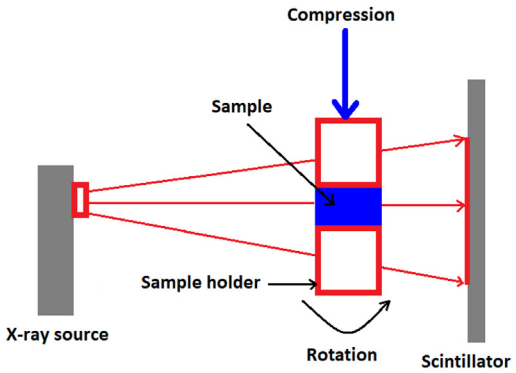

(a)

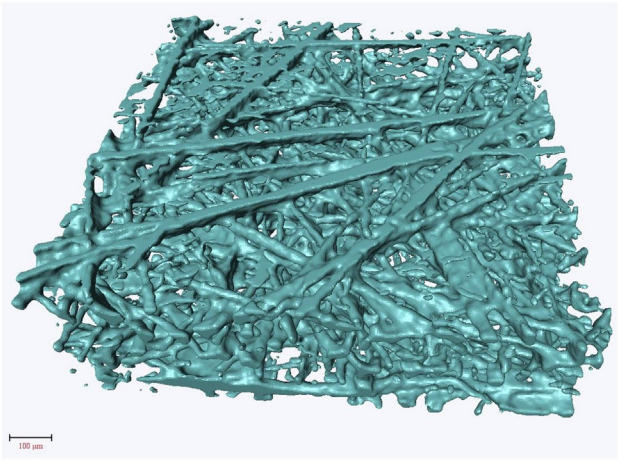

(b)

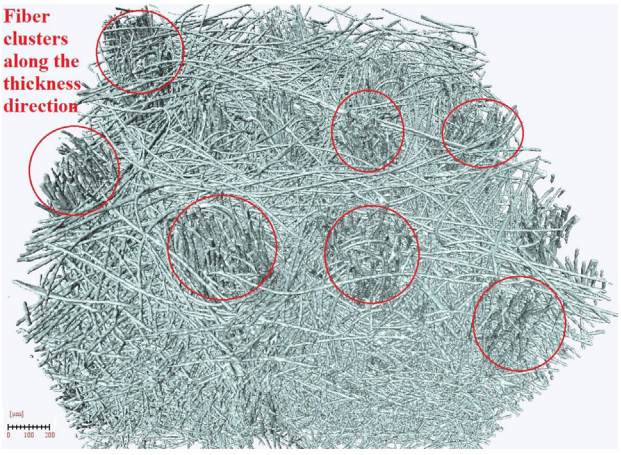

(c)

Fig. 1 – (a) Schematic of the XCT device, the reconstructed (b) paper-type and (c) felt-type GDL with CR = 0%.

The thermal resistance of the sample includes the bulk thermal resistance and the thermal contact resistance (at the surfaces between the samples and the test column). The thermal resistance of the GDL samples can be calculated as:

$$R_T = \frac{\Delta T}{Q} \tag{1}$$

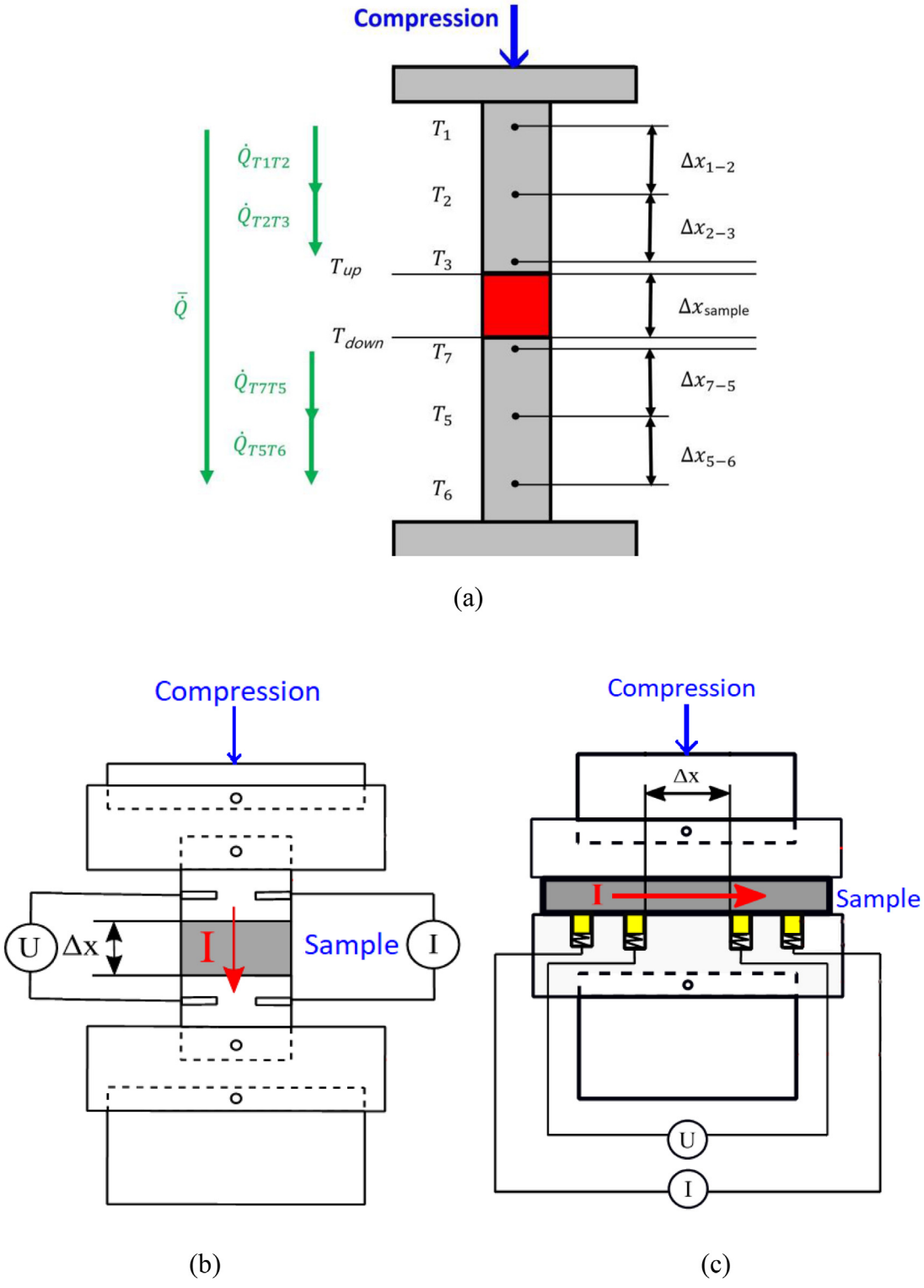

Fig. 2 – Schematic of the principles for (a) TP thermal conductivity, (b) TP electrical resistivity and (c) IP electrical resistivity measurement.

where ΔT is the temperature difference between two cross-section surfaces of the samples or the test column, Q is the heat flux flow through the surfaces. The temperature of T_1, T_2, T_3, T_5, T_6 and T_7 are measured by six thermocouples. The temperatures at the top and bottom contact surfaces, T_{up} *and* T_{down}, can be extrapolated through the measured heat flux. The distance between the thermocouples of T_1 *and* T_2, T_2 *and* T_3, T_5 *and* T_6, T_5 and T_7 is 40 mm. The distance between the points of T_3 *and* T_{up} is 0.3 mm. The distance between the points of T_7 *and* T_{down} is 0.26 mm.

The thermal conductivity considering the bulk resistance and contact resistance can be computed as:

$$\lambda = \frac{d}{R_T \cdot A} \tag{2}$$

where A is the surface area of the GDL samples, d is the thickness of the GDL samples.

The electrical resistance of the GDL samples can be calculated as:

$$R = \frac{U}{I} \tag{3}$$

where U is the voltage, and I is the current. The electrical resistivity of the GDL samples can be calculated as:

$$\rho = \frac{R \cdot A}{d} \tag{4}$$

The temperature, voltage and current during each CR test are measured at least 300 times in steady state, then the average value is calculated for each data point. It should be noted that, the thermal and electrical resistance in this paper was calculated considering the bulk and contact resistance, which reflects the real situation of the assembly for PEMFC stacks. The contact and bulk resistances are different owing to different materials and microstructures of the GDLs and BPPs, as well as different CRs. The ratio of the thermal contact resistance to the bulk resistance varied from 1 to 1.8, and both the contact and bulk resistance decreased significantly as the CR increased [41].

Numerical methods

Due to the limitations of our test conditions, it is not easy to experimentally measure the gas diffusivity and liquid water permeability. Therefore, PSM and LBM are applied to numerically calculate them instead.

Pore scale modeling

PSM was originally developed in our previous works [58–60] to compute the effective diffusivity of GDLs in the TP and IP directions. In the GDL, gas is transported through both big pores and small pores. The following Stefan-Maxwell formulas are used for calculating the gas diffusivities of O_2, H_2O and N_2, in which both Knudsen diffusion and Fick diffusion are considered.

$$\nabla x_{O_2} = \frac{RT}{p}\left(\frac{x_{O_2} j_{H_2 0} \quad x_{H_2O} j_{O_2}}{D_{O_2-H_2O}} + \frac{x_{O_2} j_{N_2} \quad x_{N_2} j_{O_2}}{D_{O_2-N_2}} \quad \frac{j_{O_2}}{D_{O_2,Kn}}\right) \tag{5}$$

$$\nabla x_{H_2O} = \frac{RT}{p}\left(\frac{x_{H_2O} j_{O_2} \quad x_{O_2} j_{H_2 0}}{D_{O_2-H_2O}} + \frac{x_{H_2O} j_{N_2} \quad x_{N_2} j_{H_2O}}{D_{H_2O-N_2}} \quad \frac{j_{H_2O}}{D_{H_2O,Kn}}\right) \tag{6}$$

$$\nabla x_{N_2} = \frac{RT}{p}\left(\frac{x_{N_2} j_{O_2} \quad x_{O_2} j_{N_2}}{D_{O_2-N_2}} + \frac{x_{N_2} j_{H_2O} \quad x_{H_2O} j_{N_2}}{D_{H_2O-N_2}} \quad \frac{j_{N_2}}{D_{N_2,Kn}}\right) \tag{7}$$

where x_i is the molar fraction of specie i ($i = O_2$, H_2 or H_2O), j_i is the flux of specie i, p is the gas pressure, R is the universal gas constant, T is the temperature, D_{i-j} is the binary diffusivity of species i and j, and D_{i-Kn} is the Knudsen diffusion coefficient of specie i. The expressions for the binary diffusion coefficient and Knudsen diffusion coefficient in this model are given in Table 1.

The conservation of oxygen is described by [62].

$$\nabla j_{O_2} = 0 \tag{8}$$

where j_{O_2} is the flux of oxygen.

To solve the above equation, the inlet and outlet surfaces are set as Dirichlet boundary conditions and the other four surfaces are set as periodic conditions. The gradient value for gas is set as 0.1 mol/m^3 [63]. The effective transport property M_{eff} of a GDL is calculated from the fluxes obtained by PSM [64], i.e.,

$$M_{eff} = \frac{j \cdot l}{b_2 \quad b_1} \tag{9}$$

where j is the flux calculated by PSM, l is the length of the computational domain, b_1 and b_2 represent the pre-described boundary conditions.

Lattice Boltzmann method

Compared to traditional computational fluid dynamics methods, LBM is a mesoscopic method that connects macroscopic and microscopic models. LBM has several advantages, such as the combination of micro-interactions, simplicity of programming, easy parallelization, and direct resolution of complex boundaries. Unlike molecule dynamics, it tracks population of particles rather than individual particles. In this work, LBM is employed to compute the liquid water permeabilities of the paper-type and felt-type GDLs.

The lattice Boltzmann equation model contains three elements, i.e., lattice structure, evolution equation and velocity distribution function of fluid particles, which can be formulated by Ref. [65]:

$$\begin{aligned} \boldsymbol{f}_i(\boldsymbol{r} + \boldsymbol{e}_i \delta t, t + \delta t) = \boldsymbol{f}_i(\boldsymbol{r}, t) \quad & Q^{-1} \Lambda_f \left(\boldsymbol{m}_f(\boldsymbol{r}, t) \quad \boldsymbol{m}_f^{eq}(\boldsymbol{r}, t)\right) \\ & + \delta t \left(I \quad \frac{1}{2} Q^{-1} \Lambda_f Q\right) \boldsymbol{G}_i(\boldsymbol{r}, t) \end{aligned} \tag{10}$$

where f is velocity distribution function at lattice location r and time t, e_i are discrete velocities, Q is a 19 × 19 matrix in this work, m_f is velocity space, and G represents body force.

In this work, D3Q19 model [26] is employed, which describes the motion process of fluid particles with 19 discrete velocities distributed on a fixed 3D lattice. The dynamic behavior of fluid is governed by [65].

$$\frac{\partial \rho \boldsymbol{u}}{\partial t} + \nabla \cdot \rho \boldsymbol{u}\boldsymbol{u} = \quad \nabla \cdot \mathbf{P} + \eta \nabla^2 \boldsymbol{u} + \mathbf{F}_b \tag{11}$$

Table 1 – Binary diffusion and Knudsen diffusion coefficients [61].

Parameters	Value ($\times 10^{-6} m^2/s$)
$D_{O_2-H_2O}$	$0.282p^{-1} \cdot (T/298.2)^{1.5}$
$D_{O_2-N_2}$	$0.220p^{-1} \cdot (T/293.2)^{1.5}$
$D_{H_2O-N_2}$	$0.293p^{-1} \cdot (T/308.1)^{1.5}$
$D_{O_2,Kn}$	$4850d \cdot (T/32)^{0.5}$
$D_{H_2O,Kn}$	$4850d \cdot (T/18)^{0.5}$
$D_{N_2,Kn}$	$4850d \cdot (T/28)^{0.5}$

and

$$\frac{\partial \varphi}{\partial t} + \nabla \cdot (\varphi \boldsymbol{u}) = \nabla \cdot (M \nabla \mu) \tag{12}$$

where ρ means mass density, u represents velocity of fluid, η represents viscosity, P is pressure gradient, F_b is body force, M is mobility parameter, φ is order parameter, and μ is chemical potential.

To calculate the permeability of porous media along the flow direction, four boundary surfaces parallel to the flow direction are set as walls, and the other two boundary surfaces are set with a pressure difference. The mathematical basis of the flow in a porous medium is Darcy's law, which can be written as [66].

$$\kappa = \frac{u_{lav} * \eta * l}{\Delta P} \tag{13}$$

where u_{lav} is the average velocity along the flow direction, l is the thickness of porous medium, $\triangle P$ means the pressure difference, and κ presents the permeability of a GDL. We fix the contact angle of 110° [67–69] and pressure drop of 1.7 (113.3 kpa).

Results and discussion

In this section, comparisons between the felt-type and paper-type GDLs are performed, including the porosity, diffusivity, permeability, thermal conductivity, electrical resistivity and mechanical strength.

Comparison of the porosity

The porosity is defined as a ratio of the pore volume inside a GDL with respect to the total volume of the GDL. The porosity decreases as CR increases for both the paper-type and felt-type GDLs, as shown in Fig. 3. The compressed GDL models are formulated based on the XCT data under different CRs. The original porosities of the felt-type and paper-type GDLs are 0.95 and 0.78, respectively. The porosity of the paper-type GDL decreases more quickly than that of the felt-type GDL as CR increases. This is because the original porosity of the paper-type GDL is much lower than that of the felt-type GDL. The porosity of the felt-type GDL decreases faster as CR > 40%. As CR increases to 60%, the porosity of the felt-type GDL is about 0.86, which is still much higher than that of the uncompressed paper-type GDL, which facilitates gas diffusion and water transport inside the GDL.

Comparison of the gas diffusivity

Gas and water are transported through the pores inside a GDL, while heat and electrons are conducted through the solid materials inside a GDL, such as fiber and binder materials. In this subsection, PSM is applied to study the impacts of compression on the effective gas diffusivity in the TP and IP directions for the compressed paper-type and felt-type GDL models using XCT data. The normalized gas diffusivity equals to the ratio of the effective diffusivity to the in-plane effective diffusivity with a compression ratio of 0%.

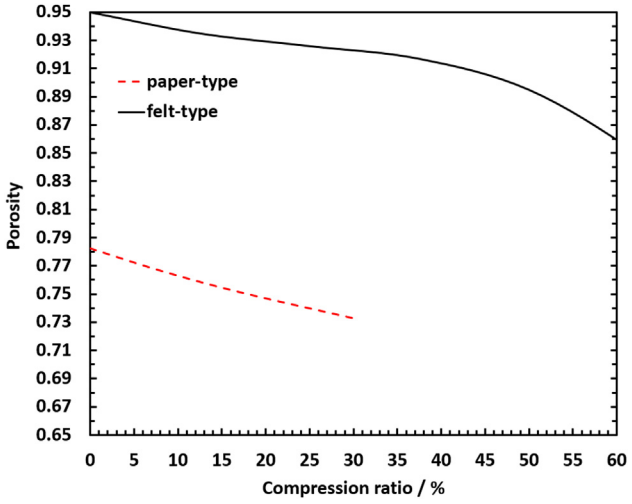

Fig. 3 – The porosities for paper-type and felt-type GDLs at different CRs.

As CR increases from 0% to 30%, gas diffusivities gradually are, respectively, decreased by 15% and 13% for the felt-type and paper-type GDLs, but the gas diffusivity for the felt-type GDL decreases faster as CR > 30%, as shown in Fig. 4. The gas diffusivity of the felt-type GDL is much greater (about 50% more) than that of the paper-type GDL, which means gas and water can be transported faster and easier inside the felt-type GDL. One can see that the gas diffusivity in the IP direction is higher than that in the TP direction, which are about 7.6% and 2.8% higher for the paper-type and felt-type GDLs, respectively. This is because the fibers are mainly oriented along the IP direction for the paper-type GDL, while the fibers are distributed in both IP and TP directions for the felt-type GDL. The felt-type GDL shows higher isotropy and better performance for gas diffusion and water transport. The gas diffusivity of the felt-type GDL with a CR of 50% is still higher than that of the paper-type GDL with a CR of 30%. The decreasing speed of gas diffusivity for the felt-type GDL is much faster

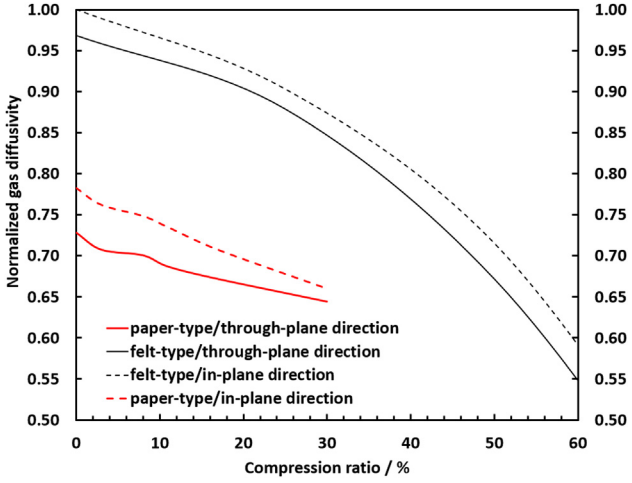

Fig. 4 – Normalized diffusivities for paper-type and felt-type GDLs at different CRs.

than that of the paper-type GDL because of their microstructural change, as shown in Fig. 9.

Comparison of the liquid water permeability

The computer code is based on Niu et al. [66] incorporating the multiple relaxation time, and LBM is employed to compute the liquid water permeability of the paper-type and felt-type GDLs. The normalized permeability equals to the ratio of the computed permeability to the permeability for the felt-type GDL with a compression ratio of 0%. Detailed descriptions of the governing equations for the LBM can be found in our previous study [65]. As CR increases from 0% to 30%, the permeability decreases by 33% and 48% for the felt-type and paper-type GDLs respectively. The permeability of the felt-type GDL changes more obviously than that of the paper-type GDL, as illustrated in Fig. 5. The permeability decreases very fast as CR<20% and 10% for the felt-type and paper-type GDLs respectively, while the decreasing speed turns to be slower as the CR is further increased. This is because the permeability sensitively depends on the size and number of big pores. As CR increases, the big pores inside the GDL are compressed to be medium or small ones, and some small pores are compressed to be closed, cutting off some pathways for water transport, as shown in Fig. 9. The permeability of the felt-type GDL is at least two times higher than that of the paper-type GDL, and the permeability of the felt-type GDL with a CR of 60% is still higher than that of the paper-type GDL with a CR of 30%. The felt-type GDL shows an absolutely better performance for water transport, which is in good accordance with other published experimental data [70]. The permeability also depends on the hydrophobic treatment, which is assumed to be the same for two types of GDLs.

Comparison of the thermal conductivity and electrical resistivity

Heat is transferred through air, fibers, binder and PTFE, while electrons are conducted by fiber and binder. In this subsection, thermal conductivity and electrical resistivity under different CRs for the paper-type and felt-type GDLs are measured and compared, as shown in Fig. 6. It should be mentioned that it is difficult to control CR accurately when CR < 10% because the surfaces of GDL microstructures are not

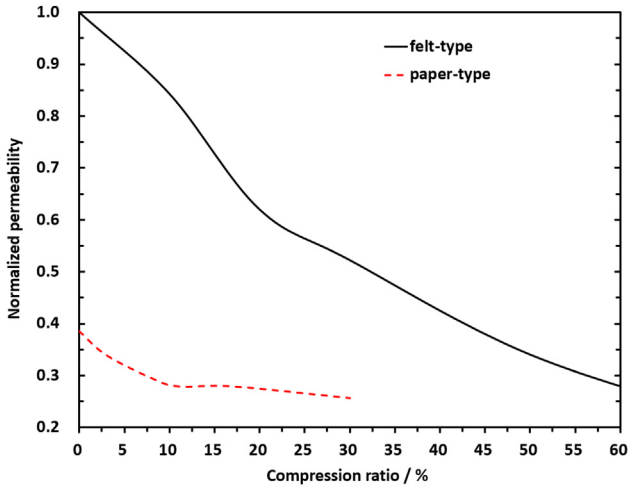

Fig. 5 – Permeabilities for paper-type and felt-type GDLs at different CRs.

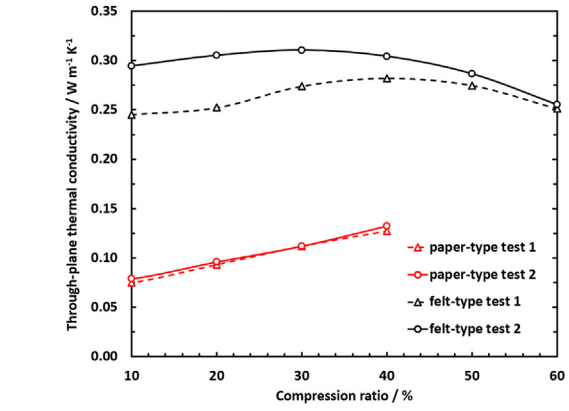

(a)

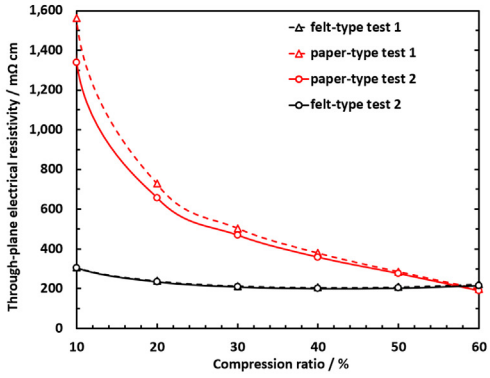

(b)

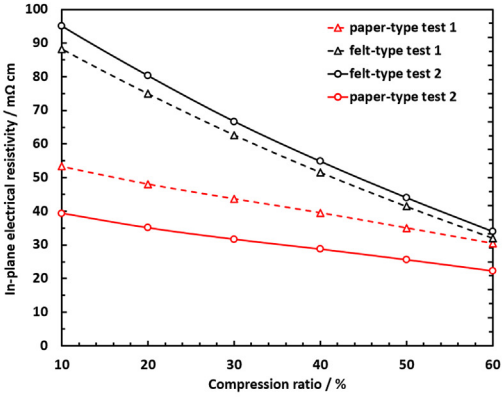

(c)

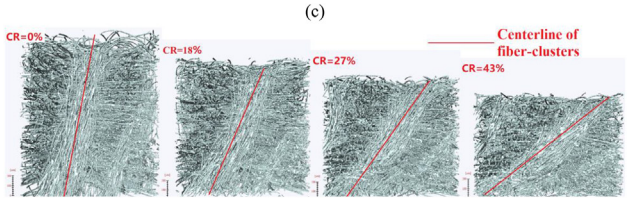

Fig. 6 – Measured (a) thermal conductivity in the TP direction, (b) electrical resistivity in the TP direction, (c) electrical resistivity in the IP direction under different CRs for paper-type and felt-type GDLs, and (d) 3D images of the carbon felt at different CRs.

flat, and the compression force is more sensitive as CR < 10%. Therefore, CR ranging from 10% to 60% is chosen for subsequent discussion in this subsection.

The thermal conductivity in the TP direction of the paper-type GDL increases linearly as CR increases, while the thermal conductivity of the felt-type GDL increases slowly as CR < 40%, as shown in Fig. 6 (a). In addition, the thermal conductivity of the felt-type GDL is at least three times higher than that of the paper-type GDL, which means that the felt-type GDL has a significantly better performance of thermal transfer. This is expected because some fiber-clusters are oriented along the TP direction for the felt-type GDL, while fibers are mainly distributed in the IP direction for the paper-type GDL. The thermal conductivity of the felt-type GDL slightly increases as CR < 40%, and then slightly decreases as CR > 40%. This phenomenon may be caused by the changed 3D microstructures of the fiber-clusters inside the felt-type GDL under high CR. One can see from Figs. 1 (c) and Fig. 6 (d) that the felt-type GDL is mainly composed of the curved fibers oriented in the IP direction and some fiber-clusters distributed along the TP direction. These fiber-clusters are compressed heavily to the IP direction as CR>40%, resulting in an increasing conductivity in the IP direction and a slightly decreasing conductivity in the TP direction.

The electrical resistivity in both the IP and TP directions decreases obviously for the paper-type GDL as CR increases, as shown in Fig. 6(b) and (c). The electrical resistivity in the TP direction of the felt-type GDL first decreases as CR increases to about 40% and then increases very slightly as CR increases from 40%. This can be also explained by the 3D microstructure changing of the fiber-clusters inside the felt-type GDL. The fiber-clusters along the TP direction are compressed obviously to the IP direction, leading to a fast-decreasing electrical resistivity in the IP direction and a slightly increasing electrical resistivity in the TP direction as CR > 40%. The electrical resistivity in the TP direction for the felt-type GDL is much lower than that of the paper-type GDL owing to the more isotropic microstructure and some fiber-clusters oriented along the TP direction. On the other hand, the electrical resistivity in the IP direction and its decreasing rate for the felt-type GDL is much higher than that of the paper-type GDL. This is because the fibers inside the paper-type GDL are mainly distributed in the IP direction layer by layer. As CR > 50%, the IP electrical resistivity of the felt-type GDL decreases to approach that of the paper-type GDL. Therefore, it is suggested to set CR to about

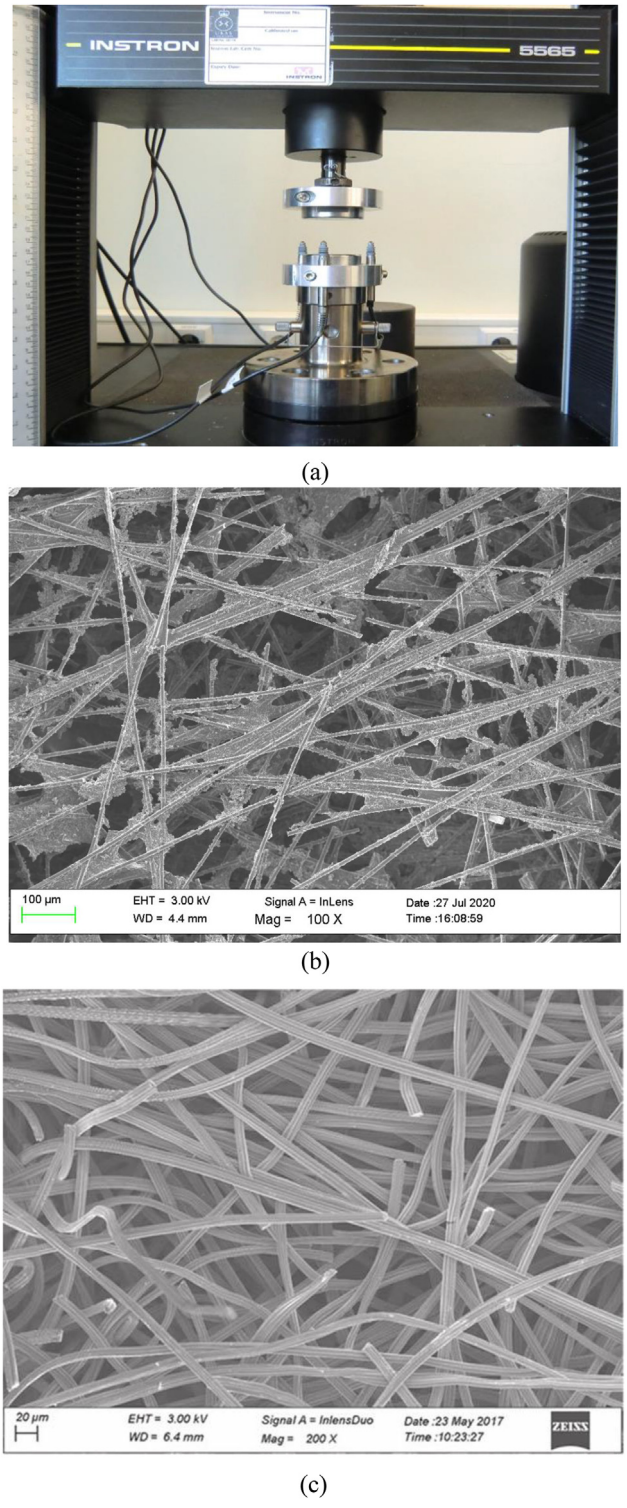

Fig. 7 – (a) Compression setup and SEM pictures of (b) paper-type GDL after compression with CR = 40%, and (c) felt-type GDL after compression with CR = 60%.

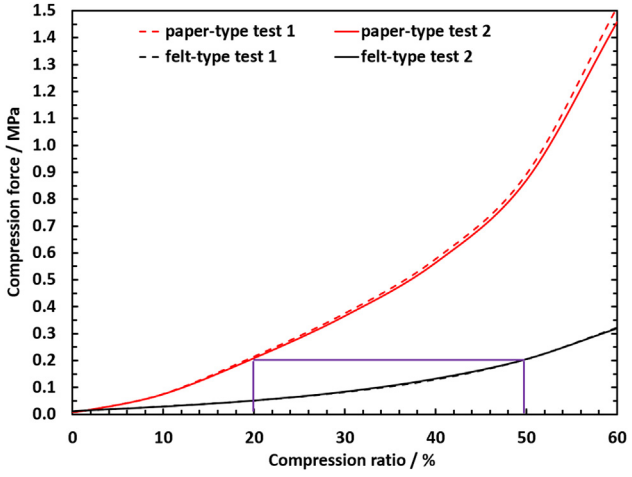

Fig. 8 – Compression force applied on paper-type and felt-type GDLs at different CRs.

50% for the felt-type GDL, or fabricate the felt-type GDL with higher bulk density.

Comparison of the mechanical strength

In this subsection, the mechanical strength of two types of GDLs are analyzed, such as the relationship between the stress and strain, which reflects the ability to resist the structural change or microstructure damage. The compression force and thickness of GDLs are controlled and measured by Instron 5565 (5 kN) setup, which combines the displacement and stress sensors, as shown in Fig. 7(a). A suitable compression force is beneficial for sealing a GDL, but an excessive force may result in some structural damage, such as broken fibers and shedding binder, as shown in Fig. 7 (b). The microstructure inside the paper-type GDL is damaged after compression with a CR of 40%, which will significantly affect the overall performance and durability of PEMFCs. The felt-type GDL shows a better ability to stop fibers from being broken after the compression with a CR of 60%, as shown in Fig. 7 (c). This is because the elasticity of the felt-type GDL is higher, which results in a higher softness of the GDL.

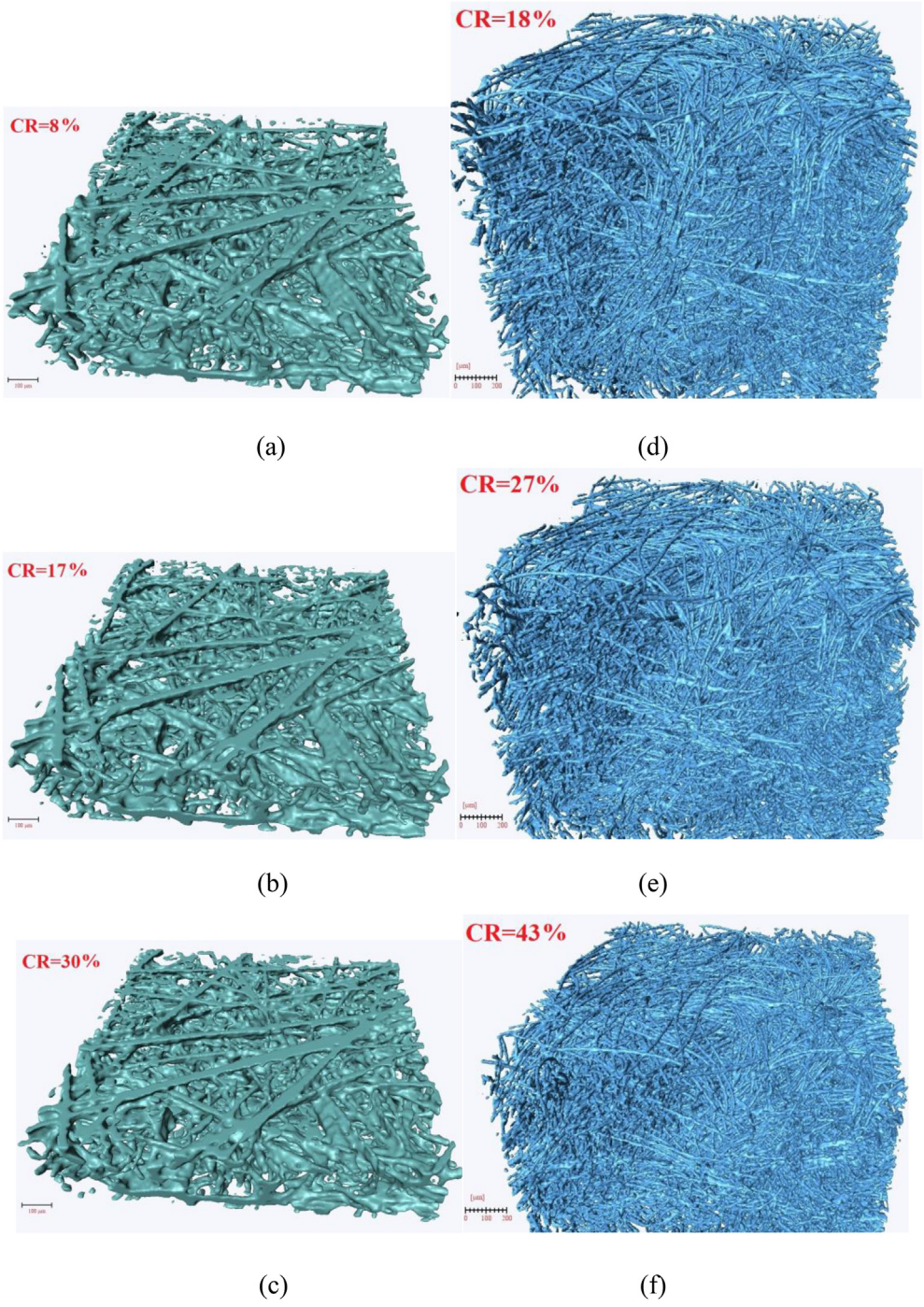

Fig. 9 – Reconstructed 3D microstructures of (a–c) paper-type and (d–f) felt-type GDLs at different CRs.

Fig. 8 shows the relationship between the compression force and CR of the paper-type and felt-type GDL samples, which reflects the mechanical response of the GDL microstructures. The compression force increases faster and faster as CR increases for both types of GDLs. This is because the bulk density among the fibers becomes higher and the resist force turns to be higher as CR increases. The increasing rate of the compression force for the paper-type GDL is significantly faster than that of the felt-type GDL. This is expected because the porosity of the paper-type GDL is much lower, resulting in a higher resistance to be compressed. As the applied compression force is set as 0.2 MPa, the CRs are 20% and 50% for the paper-type and felt-type GDLs, respectively. This is because the felt-type GDL is much more porous and easier to be compressed. The performance of gas-water transport through the channel inside the felt-type GDL will decrease significantly because more fibers will be intruded to the channel space as CR increases. Therefore, a suitable compression force is needed to balance the sealing problem and transport properties of a GDL.

Fig. 9 shows the reconstructed 3D microstructures of the paper-type and felt-type GDLs at different CRs. The felt-type GDL is more isotropic because of the curved fibers distributed in the IP direction and some fiber-clusters orientated along the TP direction. The fiber-clusters are compressed obviously to the IP direction as the CR increases. The comparison between two types of GDLs can guide microstructural design with higher mechanical strength and transport properties by combing the advantages between them. The carbon felt is suggested to be fabricated with thinner thickness and higher bulk density to increase the mechanical strength. The carbon paper is suggested to be fabricated with some fiber-clusters along the TP direction to improve the transport properties.

Conclusions

In this paper, XCT, thermal-electrical conductivity measurements, compression tests, PSM and LBM methods are combined to compare the porosity, gas diffusivity, liquid water permeability, thermal conductivity, electrical resistivity and mechanical strength of the paper-type and felt-type GDLs at different CRs. It is suggested to combine the advantages of them to balance the mechanical strength and transport properties of GDLs, such as fabricating the carbon fibers like felt-type GDL in the TP direction and paper-type GDL in the IP direction, whilst changing the porosity (bulk density) between two types of GDLs. This work can provide a new direction for microstructural optimization and performance improvement of GDLs. The main findings are summarized as follows:

(1) The porosity decreases as CR increases, and the porosity of the felt-type GDL with a CR of 60% is much higher than that of the paper-type GDL with a CR of 0%.
(2) The gas diffusivity decreases as CR increases, and the diffusivity of the felt-type GDL is approximately 50% higher than that of the paper-type GDL.
(3) The liquid water permeabilities are, respectively, decreased very fast as CR<10% and CR<20% for the paper-type and felt-type GDLs. The permeability of the felt-type GDL is at least two times higher than that of the paper-type GDL.
(4) The conductivities of the paper-type GDL increase obviously as CR increases. The conductivities of the felt-type GDL in the TP direction increase slowly as CR increases to 40% while slightly decrease as CR exceeds 40%. The TP conductivities of the felt-type GDL are significantly higher than that of the paper-type GDL.
(5) The microstructure of the paper-type GDL is damaged after compression, while the felt-type GDL shows a higher elasticity. The compression force increases faster and faster as CR increases for both types of GDLs, and the increasing rate of the paper-type GDL is much higher.

Declaration of competing interest

The authors declare that they have no known competing financial interests or personal relationships that could have appeared to influence the work reported in this paper.

Acknowledgments

The authors gratefully acknowledge financial support from the National Natural Science Foundation of China (No. 52106254), the Chinesisch-Deutsche Zentrum für Wissenschaftsförderung (M 0070), and Foshan Xianhu Laboratory of the Advanced Energy Science and Technology Guangdong Laboratory under Open-end Funds (XHD2020-004).

REFERENCES

[1] Göbel M, Godehardt M, Schladitz K. Multi-scale structural analysis of gas diffusion layers. J Power Sources 2017;355:8–17. https://doi.org/10.1016/j.jpowsour.2017.03.086.
[2] Rofaiel A, Ellis JS, Challa PR, Bazylak A. Heterogeneous through-plane distributions of polytetrafluoroethylene in polymer electrolyte membrane fuel cell gas diffusion layers. J Power Sources 2012;201:219–25. https://doi.org/10.1016/j.jpowsour.2011.11.005.
[3] El-Kharouf A, Rees NV, Steinberger-Wilckens R. Gas diffusion layer materials and their effect on polymer electrolyte fuel cell performance -ex SituandIn SituCharacterization. Fuel Cell 2014;14:735–41. https://doi.org/10.1002/fuce.201300247.
[4] Fishman Z, Hinebaugh J, Bazylak A. Microscale tomography investigations of heterogeneous porosity distributions of PEMFC GDLs. J Electrochem Soc 2010;157:B1643–50. https://doi.org/10.1149/1.3481443.
[5] Banerjee R, Hinebaugh J, Liu H, Yip R, Ge N, Bazylak A. Heterogeneous porosity distributions of polymer electrolyte membrane fuel cell gas diffusion layer materials with rib-channel compression. Int J Hydrogen Energy 2016;41:14885–96. https://doi.org/10.1016/j.ijhydene.2016.06.147.
[6] Banerjee R, Chevalier S, Liu H, Lee J, Yip R, Han K, et al. A comparison of felt-type and paper-type gas diffusion layers

for polymer electrolyte membrane fuel cell applications using X-ray techniques. J Electrochem Energy Convers Storage 2017;15. https://doi.org/10.1115/1.4037766.
[7] Escribano S, Blachot J-F, Ethève J, Morin A, Mosdale R. Characterization of PEMFCs gas diffusion layers properties. J Power Sources 2006;156:8–13. https://doi.org/10.1016/j.jpowsour.2005.08.013.
[8] Cooper NJ, Santamaria AD, Becton MK, Park JW. Neutron radiography measurements of in-situ PEMFC liquid water saturation in 2D & 3D morphology gas diffusion layers. Int J Hydrogen Energy 2017;42:16269–78. https://doi.org/10.1016/j.ijhydene.2017.05.105.
[9] Chen Y, Ke Y, Xia Y, Cho C. Investigation on mechanical properties of a carbon paper gas diffusion layer through a 3-D nonlinear and orthotropic constitutive model. Energies 2021;14. https://doi.org/10.3390/en14196341.
[10] Leng Y, Yao H, Yang D, Li B, Ming P, Zhang C. The influences of gas diffusion layer material models and parameters on mechanical analysis of proton exchange membrane fuel cell. Fuel Cell 2021;21:373–89. https://doi.org/10.1002/fuce.202100068.
[11] Ren G, Qu Z, Wang X, Zhang J. Liquid water transport and mechanical performance of electrospun gas diffusion layers. Int J Green Energy 2021;19:210–8. https://doi.org/10.1080/15435075.2021.1941046.
[12] Chen Y, Singh Y, Ramani D, Orfino FP, Dutta M, Kjeang E. 4D imaging of chemo-mechanical membrane degradation in polymer electrolyte fuel cells - Part 2: unraveling the coupled degradation mechanisms within the active area. J Power Sources 2022;520. https://doi.org/10.1016/j.jpowsour.2021.230673.
[13] Ramani D, Khattra NS, Singh Y, Orfino FP, Dutta M, Kjeang E. Mitigation of mechanical membrane degradation in fuel cells – Part 2: bonded membrane electrode assembly. J Power Sources 2021;512. https://doi.org/10.1016/j.jpowsour.2021.230431.
[14] Ramani D, Khattra NS, Singh Y, Mohseni-Javid A, Orfino FP, Dutta M, et al. Mitigation of mechanical membrane degradation in fuel cells – Part 1: gas diffusion layers with low surface roughness. J Power Sources 2021;512. https://doi.org/10.1016/j.jpowsour.2021.230446.
[15] Tötzke C, Gaiselmann G, Osenberg M, Bohner J, Arlt T, Markötter H, et al. Three-dimensional study of compressed gas diffusion layers using synchrotron X-ray imaging. J Power Sources 2014;253:123–31. https://doi.org/10.1016/j.jpowsour.2013.12.062.
[16] García-Salaberri PA, Gostick JT, Hwang G, Weber AZ, Vera M. Effective diffusivity in partially-saturated carbon-fiber gas diffusion layers: effect of local saturation and application to macroscopic continuum models. J Power Sources 2015;296:440–53. https://doi.org/10.1016/j.jpowsour.2015.07.034.
[17] Kotaka T, Tabuchi Y, Mukherjee PP. Microstructural analysis of mass transport phenomena in gas diffusion media for high current density operation in PEM fuel cells. J Power Sources 2015;280:231–9. https://doi.org/10.1016/j.jpowsour.2015.01.111.
[18] Tötzke C, Gaiselmann G, Osenberg M, Arlt T, Markötter H, Hilger A, et al. Influence of hydrophobic treatment on the structure of compressed gas diffusion layers. J Power Sources 2016;324:625–36. https://doi.org/10.1016/j.jpowsour.2016.05.118.
[19] Zenyuk IV, Parkinson DY, Connolly LG, Weber AZ. Gas-diffusion-layer structural properties under compression via X-ray tomography. J Power Sources 2016;328:364–76. https://doi.org/10.1016/j.jpowsour.2016.08.020.
[20] Eifert L, Bevilacqua N, Koble K, Fahy K, Xiao L, Li M, et al. Synchrotron X-ray radiography and tomography of vanadium redox flow batteries-cell design, electrolyte flow geometry, and gas bubble formation. ChemSusChem 2020;13:3154–65. https://doi.org/10.1002/cssc.202000541.
[21] Kulkarni N, Kok MDR, Jervis R, Iacoviello F, Meyer Q, Shearing PR, et al. The effect of non-uniform compression and flow-field arrangements on membrane electrode assemblies - X-ray computed tomography characterisation and effective parameter determination. J Power Sources 2019;426:97–110. https://doi.org/10.1016/j.jpowsour.2019.04.018.
[22] Wang Y, Wang S, Liu S, Li H, Zhu K. Three-dimensional simulation of a PEM fuel cell with experimentally measured through-plane gas effective diffusivity considering Knudsen diffusion and the liquid water effect in porous electrodes. Electrochim Acta 2019;318:770–82. https://doi.org/10.1016/j.electacta.2019.06.120.
[23] Xiao L, Luo M, Zhu L, Duan K, Bevilacqua N, Eifert L, et al. Pore-scale characterization and simulation of porous electrode material for vanadium redox flow battery: effects of compression on transport properties. J Electrochem Soc 2020;167:110545–54.
[24] Banerjee R, Bevilacqua N, Mohseninia A, Wiedemann B, Wilhelm F, Scholta J, et al. Carbon felt electrodes for redox flow battery: impact of compression on transport properties. J Energy Storage 2019;26:100997. https://doi.org/10.1016/j.est.2019.100997.
[25] Xiao L, Luo M, Zhang H, Zeis R, Sui P-C. Solid mechanics simulation of reconstructed gas diffusion layers for PEMFCs. J Electrochem Soc 2019;166:F377–85. https://doi.org/10.1149/2.0421906jes.
[26] Li M, Bevilacqua N, Zhu L, Leng W, Duan K, Xiao L, et al. Mesoscopic modeling and characterization of the porous electrodes for vanadium redox flow batteries. J Energy Storage 2020;32:101782. https://doi.org/10.1016/j.est.2020.101782.
[27] Kulikovsky A. Analytical impedance of oxygen transport in the channel and gas diffusion layer of a PEM fuel cell. J Electrochem Soc 2021;168. https://doi.org/10.1149/1945-7111/ac3a2d.
[28] Gao Y, Jin T, Wu X, Zhang T. The effect of fiber orientation on stochastic reconstruction and permeability of a carbon paper gas diffusion layer. Energies 2019;12:2808. https://doi.org/10.3390/en12142808.
[29] Gao Y. Using MRT lattice Boltzmann method to simulate gas flow in simplified catalyst layer for different inlet–outlet pressure ratio. Int J Heat Mass Tran 2015;88:122–32. https://doi.org/10.1016/j.ijheatmasstransfer.2015.04.031.
[30] Soltani P, Johari MS, Zarrebini M. Effect of 3D fiber orientation on permeability of realistic fibrous porous networks. Powder Technol 2014;254:44–56. https://doi.org/10.1016/j.powtec.2014.01.001.
[31] Nabovati A, Hinebaugh J, Bazylak A, Amon CH. Effect of porosity heterogeneity on the permeability and tortuosity of gas diffusion layers in polymer electrolyte membrane fuel cells. J Power Sources 2014;248:83–90. https://doi.org/10.1016/j.jpowsour.2013.09.061.
[32] Tayarani-Yoosefabadi Z, Harvey D, Bellerive J, Kjeang E. Stochastic microstructural modeling of fuel cell gas diffusion layers and numerical determination of transport properties in different liquid water saturation levels. J Power Sources 2016;303:208–21. https://doi.org/10.1016/j.jpowsour.2015.11.005.
[33] Kim KN, Kang JH, Lee SG, Nam JH, Kim C-J. Lattice Boltzmann simulation of liquid water transport in microporous and gas diffusion layers of polymer electrolyte membrane fuel cells. J Power Sources 2015;278:703–17. https://doi.org/10.1016/j.jpowsour.2014.12.044.
[34] Jeon DH, Kim H. Effect of compression on water transport in gas diffusion layer of polymer electrolyte membrane fuel cell

using lattice Boltzmann method. J Power Sources 2015;294:393–405. https://doi.org/10.1016/j.jpowsour.2015.06.080.
[35] Ince UU, Markötter H, George MG, Liu H, Ge N, Lee J, et al. Effects of compression on water distribution in gas diffusion layer materials of PEMFC in a point injection device by means of synchrotron X-ray imaging. Int J Hydrogen Energy 2018;43:391–406. https://doi.org/10.1016/j.ijhydene.2017.11.047.
[36] Muirhead D, Banerjee R, Lee J, George MG, Ge N, Liu H, et al. Simultaneous characterization of oxygen transport resistance and spatially resolved liquid water saturation at high-current density of polymer electrolyte membrane fuel cells with varied cathode relative humidity. Int J Hydrogen Energy 2017;42:29472–83. https://doi.org/10.1016/j.ijhydene.2017.10.031.
[37] Hollinger AS, Thynell ST. Thermal contact resistance measurements of compressed PEFC gas diffusion media. J Electrochem Energy Convers Storage 2017;13. https://doi.org/10.1115/1.4035803.
[38] Simaafrookhteh S, Taherian R, Shakeri M. Stochastic microstructure reconstruction of a Binder_Carbon Fiber_Expanded graphite carbon fiber paper for PEMFCs applications mass transport and conductivity properties. J Electrochem Soc 2019;166:F3287–99. https://doi.org/10.1149/2.0331907jes.
[39] Omrani R, Shabani B. Gas diffusion layers in fuel cells and electrolysers: a novel semi-empirical model to predict electrical conductivity of sintered metal fibres. Energies 2019;12:855. https://doi.org/10.3390/en12050855.
[40] James JP, Choi HW, Pharoah JG. X-ray computed tomography reconstruction and analysis of polymer electrolyte membrane fuel cell porous transport layers. Int J Hydrogen Energy 2012;37:18216–30. https://doi.org/10.1016/j.ijhydene.2012.08.077.
[41] Vikram A, Chowdhury PR, Phillips RK, Hoorfar M. Measurement of effective bulk and contact resistance of gas diffusion layer under inhomogeneous compression - Part I: electrical conductivity. J Power Sources 2016;320:274–85. https://doi.org/10.1016/j.jpowsour.2016.04.110.
[42] Taş M, Elden G. An experimental investigation of the effects of operating conditions on anisotropic electrical conductivity in a PEM fuel cell. Fuel Cell 2020. https://doi.org/10.1002/fuce.201900198.
[43] Tanaka S, Shudo T. Experimental and numerical modeling study of the electrical resistance of gas diffusion layer-less polymer electrolyte membrane fuel cells. J Power Sources 2015;278:382–95. https://doi.org/10.1016/j.jpowsour.2014.12.077.
[44] Todd D, Schwager M, Merida W. Three-dimensional anisotropic electrical resistivity of PEM fuel cell transport layers as functions of compressive strain. J Electrochem Soc 2015;162:F265–72. https://doi.org/10.1149/2.0611503jes.
[45] Roy Chowdhury P, Vikram A, Phillips RK, Hoorfar M. Measurement of effective bulk and contact resistance of gas diffusion layer under inhomogeneous compression – Part II: thermal conductivity. J Power Sources 2016;320:222–30. https://doi.org/10.1016/j.jpowsour.2016.04.112.
[46] Todd D, Bennett S, Merida W. Anisotropic electrical resistance of proton exchange membrane fuel cell transport layers as a function of cyclic strain. Int J Hydrogen Energy 2016;41:6029–35. https://doi.org/10.1016/j.ijhydene.2016.02.111.
[47] Yang J, Fei L, Zhang X, Ma X, Luo KH, Shuai S. Dynamic behavior of droplet transport on realistic gas diffusion layer with inertial effect via a unified lattice Boltzmann method. Int J Hydrogen Energy 2021;46:33260–71. https://doi.org/10.1016/j.ijhydene.2021.07.124.
[48] Park J, Oh H, Park H, Moon JW, Lee SJ, Jung SY. Water transport in polymer electrolyte membrane fuel cell: degradation effect of gas diffusion layer. Int J Energy Res 2022. https://doi.org/10.1002/er.7782.
[49] Shi X, Jiao D, Bao Z, Jiao K, Chen W, Liu Z. Liquid transport in gas diffusion layer of proton exchange membrane fuel cells: effects of micro-porous layer cracks. Int J Hydrogen Energy 2022;47:6247–58. https://doi.org/10.1016/j.ijhydene.2021.11.248.
[50] Csoklich C, Xu H, Marone F, Schmidt TJ, Büchi FN. Laser structured gas diffusion layers for improved water transport and fuel cell performance. ACS Appl Energy Mater 2021;4:12808–18. https://doi.org/10.1021/acsaem.1c02454.
[51] Jiang Z, Yang G, Shen Q, Li S, Liao J, Wang H, et al. Study on gas transport performance in perforated gas diffusion layer by lattice Boltzmann method. Transport Porous Media 2022;141:417–38. https://doi.org/10.1007/s11242-021-01726-8.
[52] Yin B, Xu S, Yang S, Dong F. Influence of microelliptical groove gas diffusion layer (GDL) on transport behavior of proton exchange membrane fuel cell (PEMFC). Int J Heat Mass Tran 2021;180. https://doi.org/10.1016/j.ijheatmasstransfer.2021.121793.
[53] Wang XL, Qu ZG, Lai T, Ren GF, Wang WK. Enhancing water transport performance of gas diffusion layers through coupling manipulation of pore structure and hydrophobicity. J Power Sources 2022;525. https://doi.org/10.1016/j.jpowsour.2022.231121.
[54] Zapardiel D, García-Salaberri PA. Modeling the interplay between water capillary transport and species diffusion in gas diffusion layers of proton exchange fuel cells using a hybrid computational fluid dynamics formulation. J Power Sources 2022;520. https://doi.org/10.1016/j.jpowsour.2021.230735.
[55] Aldakheel F, Ismail MS, Hughes KJ, Ingham DB, Ma L, Pourkashanian M. Effects of compression on mechanical integrity, gas permeability and thermal stability of gas diffusion layers with/without sealing gaskets. Int J Hydrogen Energy 2021;46:22907–19. https://doi.org/10.1016/j.ijhydene.2021.04.087.
[56] Lee S-H, Kim HM. Effects of rib structure and compression on liquid water transport in the gas diffusion layer of a polymer electrolyte membrane fuel cell. J Mech Sci Technol 2022;36:235–46. https://doi.org/10.1007/s12206-021-1222-8.
[57] Moslemi M, Javaherdeh K, Ashorynejad HR. Effect of compression of microporous and gas diffusion layers on liquid water transport of PEMFC with interdigitated flow field by Lattice Boltzmann method. Colloids Surf A Physicochem Eng Asp 2022;642. https://doi.org/10.1016/j.colsurfa.2022.128623.
[58] Lange KJ, Sui P-C, Djilalia N. Pore scale simulation of transport and electrochemical reactions in reconstructed PEMFC catalyst layers. J Electrochem Soc 2010;157(10):B1434–42. https://doi.org/10.1149/1.3478207.
[59] Lange KJ, Sui P-C, Djilali N. Pore scale modeling of a proton exchange membrane fuel cell catalyst layer: effects of water vapor and temperature. J Power Sources 2011;196:3195–203. https://doi.org/10.1016/j.jpowsour.2010.11.118.
[60] Lange KJ, Sui P-C, Djilali N. Determination of effective transport properties in a PEMFC catalyst layer using different reconstruction algorithms. J Power Sources 2012;208:354–65. https://doi.org/10.1016/j.jpowsour.2011.11.001.
[61] Lange KJ, Sui P-C, Djilali N. Using an ILU/deflation preconditioner for simulation of a PEM fuel cell cathode catalyst layer. Commun Comput Phys 2015;14:537–73. https://doi.org/10.4208/cicp.180412.301012a.
[62] Zhu L, Zhang H, Xiao L, Bazylak A, Gao X, Sui P-C. Pore-scale modeling of gas diffusion layers: effects of compression on transport properties. J Power Sources 2021;496. https://doi.org/10.1016/j.jpowsour.2021.229822.

[63] Zhang H, Zhu L, Harandi HB, Duan K, Zeis R, Sui P-C, et al. Microstructure reconstruction of the gas diffusion layer and analyses of the anisotropic transport properties. Energy Convers Manag 2021;241:114293. https://doi.org/10.1016/j.enconman.2021.114293.

[64] Zhu L, Yang W, Xiao L, Zhang H, Gao X, Sui P-C. Stochastically modeled gas diffusion layers: effects of binder and polytetrafluoroethylene on effective gas diffusivity. J Electrochem Soc 2021;168:014514. https://doi.org/10.1149/1945-7111/abdc60.

[65] Duan K, Zhu L, Li M, Xiao L, Bevilacqua N, Eifert L, et al. Multiphase and pore scale modeling on catalyst layer of high-temperature polymer electrolyte membrane fuel cell. J Electrochem Soc 2021;168. https://doi.org/10.1149/1945-7111/abff03.

[66] Niu X-D, Munekata T, Hyodo S-A, Suga K. An investigation of water-gas transport processes in the gas-diffusion-layer of a PEM fuel cell by a multiphase multiple-relaxation-time lattice Boltzmann model. J Power Sources 2007;172:542–52. https://doi.org/10.1016/j.jpowsour.2007.05.081.

[67] Sabharwal M, Gostick JT, Secanell M. Virtual liquid water intrusion in fuel cell gas diffusion media. J Electrochem Soc 2018;165:F553–63. https://doi.org/10.1149/2.0921807jes.

[68] Gurau V, Bluemle MJ, De Castro ES, Tsou Y-M, Mann JA, Zawodzinski TA. Characterization of transport properties in gas diffusion layers for proton exchange membrane fuel cells. J Power Sources 2006;160:1156–62. https://doi.org/10.1016/j.jpowsour.2006.03.016.

[69] Cetinbas FC, Ahluwalia RK, Shum AD, Zenyuk IV. Direct simulations of pore-scale water transport through diffusion media. J Electrochem Soc 2019;166:F3001–8. https://doi.org/10.1149/2.0011907jes.

[70] Chuang P-YA, Rahman MA, Mojica F, Hussey DS, Jacobson DL, LaManna JM. The interactive effect of heat and mass transport on water condensation in the gas diffusion layer of a proton exchange membrane fuel cell. J Power Sources 2020;480. https://doi.org/10.1016/j.jpowsour.2020.229121.